



Weld Solidification and Cracking Behavior of Free-Machining Stainless Steel

A range of alloy compositions exhibiting good resistance to solidification cracking is identified

BY J. A. BROOKS, C. V. ROBINO, T. J. HEADLEY, AND J. R. MICHAEL

ABSTRACT. The weld solidification and cracking behavior of sulfur-bearing, free-machining austenitic stainless steel was investigated for both gas tungsten arc (GTA) and pulsed laser beam welding processes. The GTA weld solidification was consistent with that predicted with existing solidification diagrams, and the cracking response was controlled primarily by the solidification mode. The solidification behavior of the pulsed laser welds was complex and often contained regions of primary ferrite and primary austenite solidification, although in all cases the welds were found to be completely austenite at room temperature. Electron backscattered diffraction (EBSD) pattern analysis indicated the nature of the base metal at the time of solidification plays a primary role in initial solidification. The solid-state transformation of austenite to ferrite at the fusion zone boundary and ferrite to austenite on cooling may both be massive in nature. A range of alloy compositions that exhibited good resistance to solidification cracking and was compatible with both welding processes was identified. The compositional range is bounded by laser weldability at lower Cr_{eq}/Ni_{eq} ratios and by the GTA weldability at higher ratios. It was found with both processes that the limiting ratios were somewhat dependent upon sulfur content.

Introduction

The austenitic stainless steels with minor additions of sulfur, selenium, or lead can exhibit superior machinability with improved surface finishes, reduction in burring, and higher cutting rates. These

J. A. BROOKS is with Sandia National Laboratories, Livermore, Calif. C. V. ROBINO, T. J. HEADLEY, and J. R. MICHAEL are with Sandia National Laboratories, Albuquerque, N. Mex.

alloying elements form second-phase particles that act as lubricants and enhance chip removal during the machining process. The most widely used free-machining stainless steel is AISI 303, in which sulfur is used at levels as high as 0.4 wt-%. This level is an order of magnitude higher than the maximum allowable sulfur in AISI 304L of the same basic composition. Concerns regarding the effect of these high-sulfur contents on weld fabrication and performance has limited the use of sulfur-based stainless steels in applications involving welding.

It is recognized sulfur can be extremely detrimental to weldability, especially in the formation of solidification hot cracks. However, Vareststraint testing of 303 stainless steel by Lundin et al. (Ref. 1) indicated high levels of sulfur can be tolerated without cracking if the weld solidifies as primary ferrite, while little sulfur can be tolerated if the weld solidifies as primary austenite. Brooks et al. (Ref. 2) showed similar behavior in Fe-Ni-Cr ternary alloys with high levels of both sulfur and phosphorus. In conventional welding processes such as GTA and shielded metal arc (SMA), the change in solidification mode from primary austenite to primary ferrite occurs at a Cr_{eq}/Ni_{eq} ratio of ~ 1.4 when using the equivalents of the WRC 92 diagram (Ref. 3). This ratio is $\sim 1.50-1.55$

(Refs. 4-6) when using Hammar and Svensson equivalents (Ref. 7). For compositions with Cr_{eq}/Ni_{eq} ratios below these values, the welds typically solidify as primary austenite, whereas, above these values, solidification occurs as primary ferrite. Other factors such as solidification velocity can, however, affect the solidification behavior.

Little data are available on high-energy-density (HED) welds of the free-machining austenitic stainless steels. It is known that with the high-solidification velocities common with these processes, the transition in solidification mode from primary ferrite to primary austenite occurs at higher Cr_{eq}/Ni_{eq} ratios than those given above, and this is due to dendrite tip undercooling (Refs. 8-21). Dendrite tip undercooling increases with increasing velocity for both ferrite and austenite, but the rate of this increase is greater for ferrite. Thus, a critical solidification velocity can exist above which the austenite phase will solidify at a higher temperature than that of ferrite, and it, therefore, becomes the stable solidification phase. This critical velocity for transition from primary ferrite to primary austenite is dependent on composition (Refs. 13, 16, 20). In a manner similar to the more conventional welding processes, the role of the solidification mode is very important in the weld cracking behavior during HED processing (at least with nominal levels of P and S Refs. 22-24). It must also be recognized that the solidification and solid state transformation behavior can be considerably different between the HED welding processes and the more conventional GTA and SMA welding processes (Refs. 9-21).

In the manufacturing of engineering components, it is common to use several welding processes. One region of a component may require a GTA weld and another region a laser beam (LB) weld in the

KEY WORDS

Sulfur Bearing
Stainless Steel
Laser Beam Welding
Gas Tungsten Arc
Solidification
Free Machining
Cracking

Table 1 — Alloy Compositions (wt-%) and Calculated Cr_{eq}/Ni_{eq} Ratios

Heat No.	1	2	3	4	5	6	7	8	9	10
C	0.03	0.03	0.03	0.03	0.03	0.03	0.03	0.03	0.03	0.03
Mn	1.48	1.49	1.48	1.49	1.48	1.48	1.47	1.48	1.49	1.47
Si	0.62	0.59	0.62	0.61	0.57	0.57	0.59	0.61	0.59	0.61
P	0.03	0.03	0.03	0.03	0.03	0.03	0.03	0.03	0.03	0.03
S ^(a)	0.04	0.04	0.04	0.11	0.27	0.42	0.11	0.12	0.27	0.18
Cr ^(a)	17.55	19.18	18.37	18.45	18.47	18.45	16.87	17.78	17.77	18.16
Ni ^(a)	10.51	8.92	9.73	8.60	8.49	8.61	10.08	9.29	9.30	8.83
Mo	0.35	0.35	0.35	0.35	0.35	0.35	0.35	0.35	0.35	0.35
Cu	0.31	0.30	0.30	0.30	0.30	0.30	0.30	0.31	0.30	0.30
N	0.02	0.02	0.02	0.02	0.02	0.02	0.02	0.02	0.02	0.02
Cr_{eq}/Ni_{eq} (WRC92)	1.48	1.89	1.67	1.85	1.87	1.85	1.48	1.67	1.67	1.78
Cr_{eq}/Ni_{eq} (H and S)	1.55	1.95	1.73	1.92	1.94	1.92	1.55	1.74	1.74	1.85

(a) AISI allowable composition of 303: Ni: 8–10%, Cr: 17–19%, S: 0.15% min.

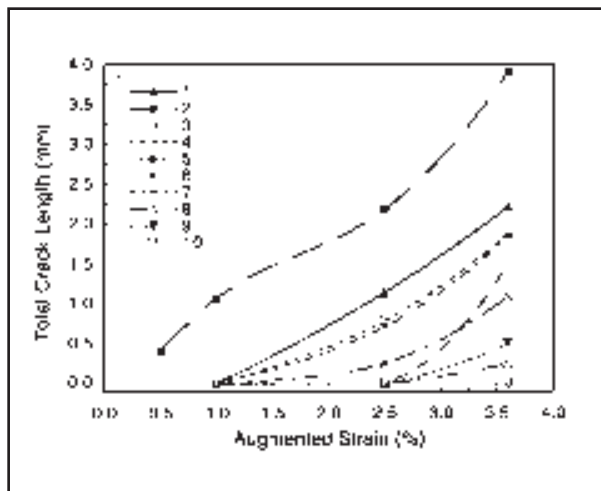


Fig. 1 — Varestraint results showing total crack length vs. augmented strain.

same material. In other cases, one heat of material or one material specification may be used for the manufacturing of a variety of components. Thus, alloy compositions that exhibit good weldability for both processes would be very desirable. A goal of this investigation was to study the effect of sulfur content and solidification behavior on the weld cracking susceptibility of both GTA and pulsed YAG laser beam welding (LBW) in 303 type stainless steel and to identify any differences that may exist between the two processes. Summaries of these studies, including weld property data, have been reported elsewhere (Refs. 25, 26)

Experiments

Ten experimental heats were induction melted, cast, and hot rolled into strips

~ 7.6 cm wide and 3.2 mm thick. Chromium and nickel contents were adjusted to provide a range of Cr_{eq}/Ni_{eq} ratios. Sulfur content was also varied while other minor alloying elements and impurities were held constant. The alloy compositions and heat designations are shown in Table 1. It can be seen that some of the materials are equivalent to 304L with high levels of sulfur, and others are characteristic of the 303 free-machining grade with sulfur additions as high as 0.4 wt-%. Table 1 shows the Cr_{eq}/Ni_{eq} ratios calculated using the equivalents of both Hammar and Svensson

and the WRC 92 diagram. However, for subsequent discussion, the Hammar and Svensson equivalents are used, and compositions are given in wt-%.

Subsize Varestraint testing (Ref. 27) was used to determine the susceptibility to solidification cracking of the GTA welds. Composite samples were made by cutting 2.5-cm-wide strips across the width of the alloy sheets and electron beam (EB) welding these to 304L end tabs. The composite specimens were 3.2 mm thick, 2.54 cm wide, and 16.5 cm long. Weld parameters used for the Varestraint test were 90 A, 12 V, and 3 mm/s travel speed with argon shielding. Duplicate samples were run at augmented strains over a range of 0.5 to 3.6%. Crack lengths were measured at 30X magnification on the as-welded samples.

Autogenous circular welds with a diameter of 1 cm were used to assess the

cracking susceptibility of pulsed YAG laser welds. Two weld schedules were used, one at 20 Hz, 20 W, and 3.4 mm/s (8 in./min) using 2.5 J/pulse and the other at 30 Hz, 75 W, and 4.6 mm/s (11 in./min) using 3.7 J/pulse. Single-pulse weld cracking susceptibility was also conducted using a Weeter-type test (Ref. 28) with a hole diameter of 0.483 mm and hole depths ranging from 0.203 to 0.508 mm.

Samples for metallographic examination were polished and etched with oxalic acid, and samples for transmission electron microscopy (TEM) analysis were thinned using a perchloric acid polishing solution.

Electron backscattered diffraction (EBSD) was used to study the crystallographic orientation of individual grains in the weld metal. Electron backscattered diffraction was performed in a JEOL 6400 or a JEOL 5900LV scanning electron microscope (SEM). Samples for EBSD were prepared by standard metallographic practice followed by light electrolytic etching in oxalic acid or electropolishing in a perchloric acid solution. Electron backscattered diffraction was conducted at an accelerating voltage of 20 kV with a 70-deg sample tilt. It is possible to map the orientation of many grains using EBSD. This was accomplished with the Noran Instruments Orkid system. Automated orientation mapping with EBSD is done by the automated acquisition and analysis of EBSD patterns for each pixel in an image. In this study the samples were scanned with grids of 200 x 200 pixels.

Results

GTA Welds

The GTA weld Varestraint results are shown plotted as total crack length vs. augmented strain in Fig. 1. The crack length reported is the average of duplicate tests at each strain. It can be seen there is a large range in cracking behavior. Heat 2 is seen to be by far the most susceptible to solidification cracking, whereas Heats 5 and 10 are extremely resistant to cracking (exhibited no cracking even at the highest strain of 3.6%). Table 2 shows the maximum crack length as a function of augmented strain for the same set of tests. At all strain levels, the maximum crack length is greatest again for Heat 2 (Cr_{eq}/Ni_{eq} ratio of 1.95 and sulfur content of 0.039%). It can also be seen for Heats 1, 4, 6, 7, and 9 that the maximum crack lengths at the highest level of strain tested, 3.6%, are approximately the same. However, their cracking behavior at the lower strain levels is considerably different. The cracking response will be related to solidification mode and microstructure in a later section.

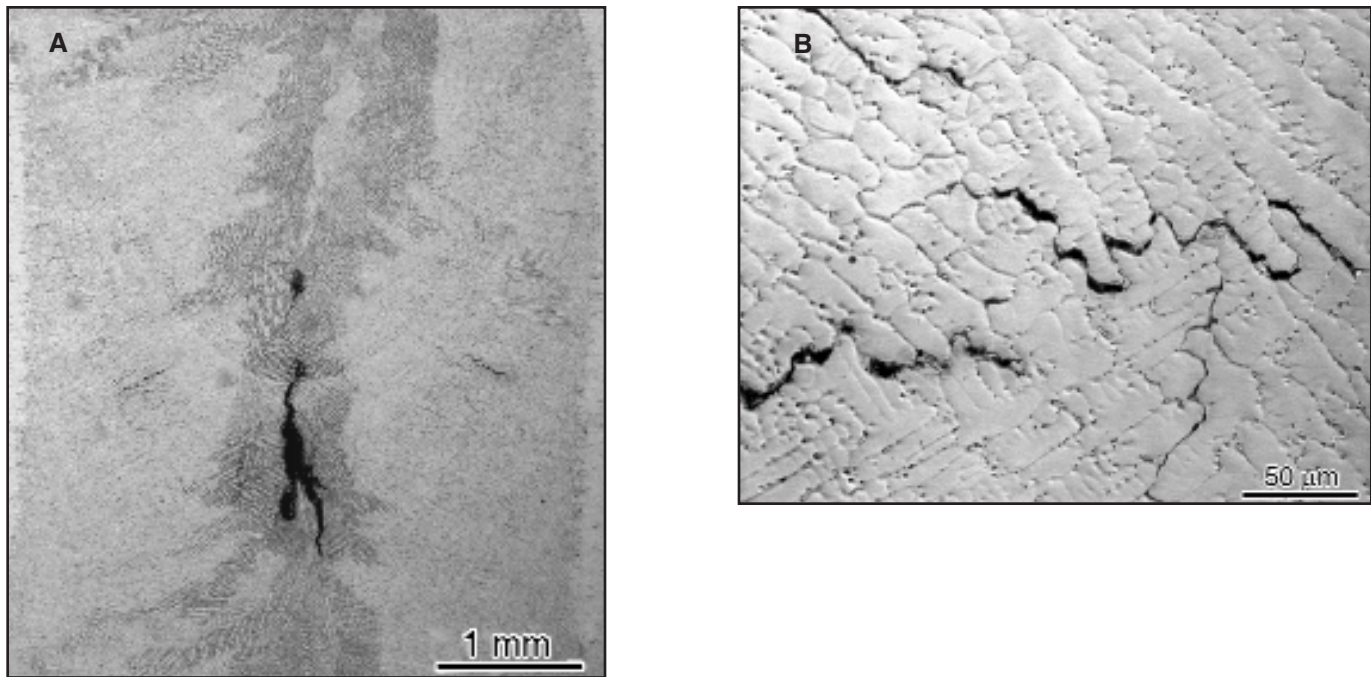


Fig. 2 — A — Solidification and cracking behavior of Heat 7 containing 0.11% S with a Cr_{eq}/Ni_{eq} ratio of 1.55, dark etching regions solidified as primary austenite, lighter regions as primary ferrite; B — higher magnification showing cracks in region of primary austenite solidification.

The alloys can be separated into three groups to describe their solidification behavior. Alloys with a Cr_{eq}/Ni_{eq} ratio of 1.55 (Heats 1 and 7) generally solidified as primary ferrite (F/A) but did exhibit some regions of primary austenite solidification with small amounts of eutectic ferrite (A/F). Figure 2A shows the overall solidification structure and cracking behavior of Heat 7 (0.11% S). The darker etching regions located primarily near the weld centerline solidified as primary austenite, and the lighter etching regions as primary ferrite. It can be seen cracking occurred in both regions. The higher magnification micrograph in Fig. 2B shows cracks in the primary austenite solidified region. The dark etching spherical particles were identified as sulfides and are primarily located in the interdendritic regions of the structure. The cracking behavior of Heat 1 (with the same Cr_{eq}/Ni_{eq} ratio as Heat 7 but a lower sulfur content of 0.039%) is shown in Fig. 3A. This weld generally solidified as primary ferrite, but many of the grain boundary regions solidified as austenite, as shown at higher magnification in Fig. 3B. This microstructure and cracking behavior was similar in Heats 7 and 1 in the regions of F/A solidification. A SEM micrograph of the region ahead of the crack in Heat 7 is shown in Fig. 3C. The cracks are present along austenite solidification grain boundaries and are associated with sulfides. The small spherical sulfides segregated at the cell boundaries and ahead of a crack tip (some of which

Table 2 — Maximum Crack Length (mm)

Heat No. Strain	1	2	3	4	5	6	7	8	9	10
0.5%		5								
1.0%	0	15	0	0	0	0	13	8	0	0
2.5%	10	15	0	11	0	10	11	13	0	0
3.6%	13	18	8	15	0	15	15	8	15	0

have been etched away during metallographic preparation) are clearly visible in Fig. 3C. It was found by SEM EDS analysis that the sulfides contain Mn and Cr. Some eutectic ferrite is also apparent in Fig. 3C. It appears the regions local to the grain boundaries were sufficiently modified in composition by segregation and/or backfilling with Ni- and S-enriched liquid during Varestraint testing to result in austenitic solidification with eutectic ferrite (A/F).

The second group of alloys is those with a Cr_{eq}/Ni_{eq} ratio in the range of 1.73–1.85 (Heats 3, 8, 9, and 10). These alloys solidified as primary ferrite and exhibited a skeletal ferrite morphology with some regions of lathy ferrite. An example of this microstructure is shown in Fig. 4A for Heat 10 with a Cr_{eq}/Ni_{eq} ratio of ~1.85, tested at a strain of 1%. This heat did not crack at any strain level tested. The micrograph was taken near the trailing edge of the weld pool where cracking would be expected in the Varestraint test. The different etching behavior of the grain

boundary regions is a result of highly localized strain and possibly backfilling during testing. One such region is shown at higher magnification in the SEM image of Fig. 4B. A large concentration of sulfide particles are evident at the ferrite / austenite boundaries, in the solidification cell boundaries, and especially in the grain boundary regions that exhibited the different etching behavior.

The third group of alloys is those with Cr_{eq}/Ni_{eq} ratios in the range of 1.92 to 1.95. The microstructure of Heat 2 (Cr_{eq}/Ni_{eq} ratio ~1.95) is shown in Fig. 5A. Much of the microstructure is characteristic of welds that solidify completely as ferrite and then transform to austenite at a temperature considerably below that of final solidification (Refs. 9, 29, 30). In this case, the ferrite exhibits a more lath-type structure in which the laths can extend across a number of solidification cell diameters thereby masking the cell boundaries. The grain boundary crack shown in the micrograph is typical of alloys in this group and occurred when tested at an aug-

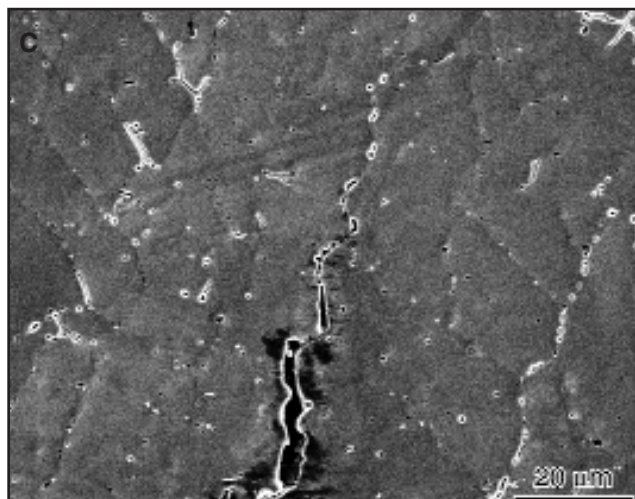
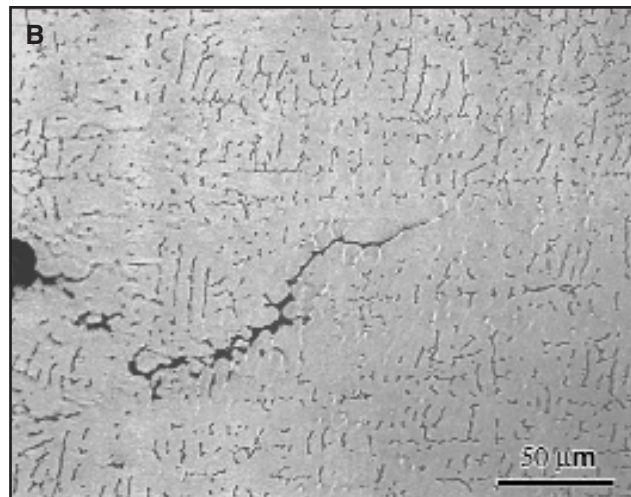
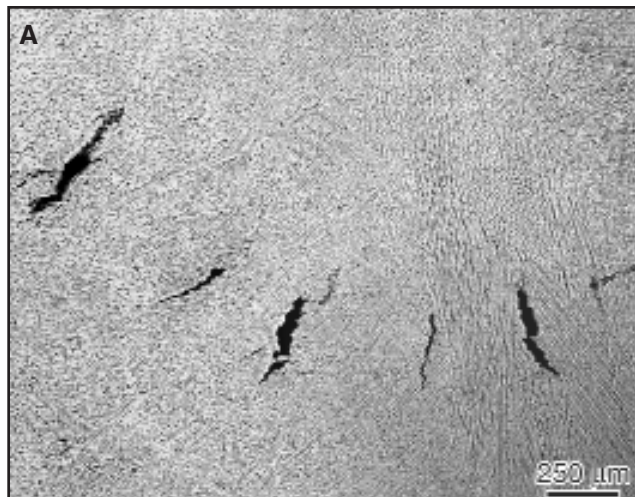


Fig. 3 — A — Solidification and cracking behavior of Heat 1 containing 0.04% S with a Cr_{eq}/Ni_{eq} ratio of 1.55; B — higher magnification showing primary ferrite solidified structure except in region of crack where final solidification occurred as austenite; C — SEM image showing Mn and Cr containing sulfides with some eutectic ferrite in cell boundaries.

mented strain of 2.5%. At higher magnification (Fig. 5B), the grain boundary regions are more apparent and are seen to contain little ferrite and a large concentration of sulfides (even at the low sulfur level of 0.039%). Although Heat 2 has one of the lowest levels of sulfur, it exhibited the most severe cracking of all the heats studied. In heats with this high Cr_{eq}/Ni_{eq} ratio, but with the higher levels of sulfur, the microstructures appeared to be more characteristic of F/A solidification (more similar to that in Fig. 4).

Laser Weld Evaluation

The cracking behavior of laser welds made with both weld schedules was assessed by metallographically examining transverse cross sections every 90 deg in the circular welds. It was found the two heats with a Cr_{eq}/Ni_{eq} ratio of ~ 1.55

(Heats 1 and 7) exhibited severe cracking. The sulfur contents of these heats are 0.04 and 0.11%. Heat 9 (Cr_{eq}/Ni_{eq} ratio ~ 1.74 , sulfur level = 0.27%) was the only other heat to exhibit cracking in these tests, and the cracking was much less severe than in Heats 1 and 7. The other two heats with the same Cr_{eq}/Ni_{eq} ratios similar to Heat 9 but lower levels of sulfur, 0.04% and 0.12%, did not exhibit cracking. Cracking was not observed at any sulfur level in the heats with the highest Cr_{eq}/Ni_{eq} ratios of 1.85 to 1.95.

The cracking behavior of all laser welds is plotted in Fig. 6 for different impurity levels (P+S) and Cr_{eq}/Ni_{eq} ratios. Also shown are results of the original diagram of Pacary et al. (Refs. 22, 23) for 304L stainless steel and those of Lienert (Ref. 24) for 304L and 316L. Note that the (P+S) levels of their studies are typical of the low-carbon grades of austenitic stainless steels. The lines separating the region of cracking and no cracking are a compilation of all the data. The justification for plotting the results in terms of combined phosphorus and sulfur level is based more on convention than on experimental data (Refs. 5, 31–33). It is recognized both elements can form low melting liquids that can lead to solidification cracks, but the potency of each element may well be different. It was found in GTA welds of Fe-Ni-Cr ternary alloys that phosphorus was more detrimental to solidification cracking response than sulfur (Refs. 2, 9). This

difference was related to the nature of the eutectic liquids, i.e., phosphides formed films that more readily wet the solidifying boundaries, whereas sulfides tended to form as spherical droplets. The effect of these two elements on both HAZ and solidification cracking is still an area of active research (Ref. 34). Since the goal of our work was to determine the effect of sulfur level, the phosphorus level was held constant and near the upper extreme of typical austenitic stainless steel specifications. In this way, our results should represent worst case behavior for a particular level of sulfur in Type 303 alloy, but it must be recognized phosphorus may be influencing the cracking behavior. It can be seen in Fig. 6 that the results of this study are consistent with those of the other two investigators. Only the heat with a Cr_{eq}/Ni_{eq} ratio of 1.74 and a high level of (P+S) would reflect any change to the earlier diagrams (Refs. 22, 24). It should also be noted not all the heats are clearly defined by the line separating cracking from no cracking. This is not surprising and is similar to results reported for GTA welds (Refs. 5, 35).

Laser welds were evaluated using light microscopy, scanning electron microscopy (SEM), and TEM techniques. All welds consisted of single-phase austenite with no detectable ferrite. Although the laser weld solidification behavior and microstructures were considerably different from the GTA welds, in general they can also be separated into three groups based on Cr_{eq}/Ni_{eq} ratio. Alloys with a Cr_{eq}/Ni_{eq} ratio of 1.55 (Heats 1 and 7) solidified completely as austenite. The austenite solidification structure and severe cracking behavior of Heat 7 with 0.11 sulfur is shown in the low-magnification micrograph in Fig. 7A. The higher magnification image of Fig. 7B shows the very distinct cellular solidification structure typical of primary austenite, with weld cracks confined to the austenite grain

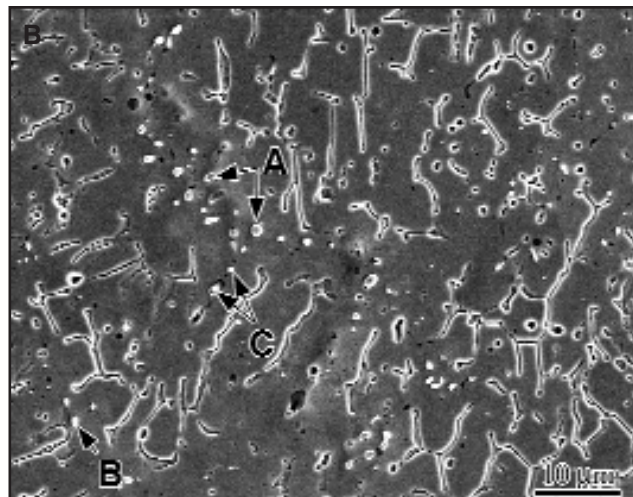
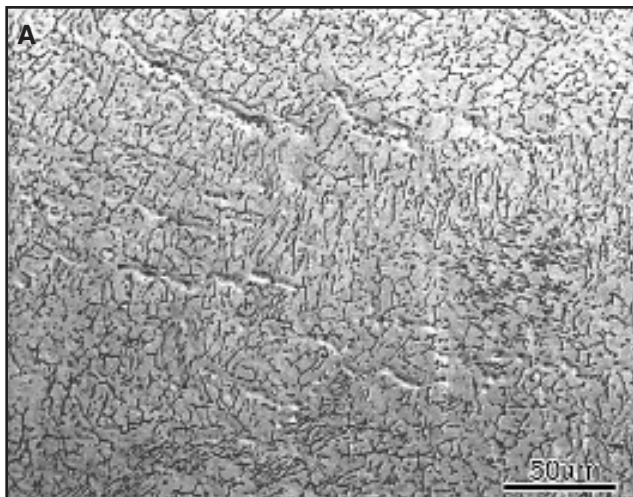


Fig. 4 — Heat 10 $Cr_{eq}/Ni_{eq} = 1.85$ tested at 1% strain. A — Primary ferrite solidified structure exhibiting both skeletal and lathy ferrite morphologies characteristic of alloys with Cr_{eq}/Ni_{eq} ratios of 1.73–1.85, note: evidence of high strain in grain boundary regions resulting from Vareststraint test; B — SEM image showing large sulfide particles at solidification grain boundary (A), ferrite/austenite interface (B), and cell boundaries (C).

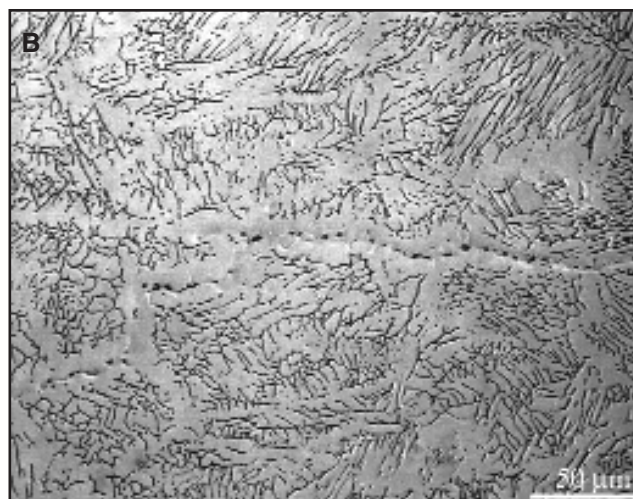
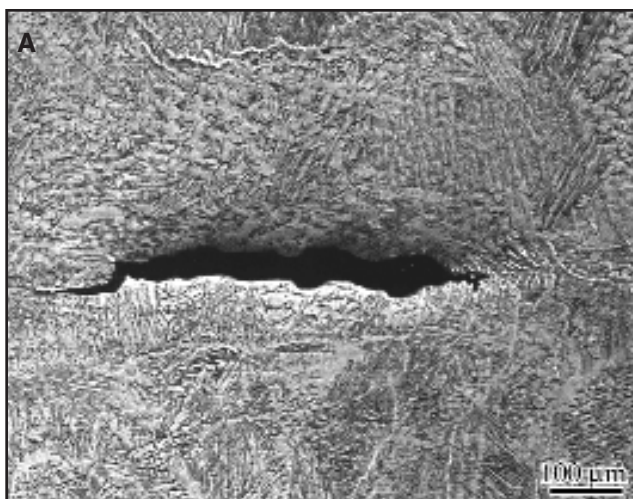


Fig. 5 — A — Microstructure of Heat 2 typical of GTA welds in heats with Cr_{eq}/Ni_{eq} ratios of 1.92–1.95. Sample tested at 2.5% strain exhibiting a crack and a lathy ferrite morphology; B — higher magnification showing sulfides in grain boundary region.

boundaries. It is interesting to note the grain or subgrain size appears smaller than is apparent at the lower magnification in Fig 7A.

A STEM image from a weld in Heat 1, Cr_{eq}/Ni_{eq} ratio of 1.55, which contains 0.04% sulfur, is shown in Fig. 8. In this micrograph, the cellular solidification structure resulting from microsegregation is also very evident. However, the degree of microsegregation was small with a measured cell boundary enrichment in Cr and Ni of only ~1 wt-%. The particles noted with the arrows marked with “O” are amorphous Al-containing oxides, and the particles marked with “P” are Cr-containing phosphides. However, no sulfides were observed in the cell boundaries of TEM samples at this sulfur level (0.04%).

The composition in regions of cracking

in Heat 7 was examined using energy-dispersive spectrometry and spectrum imaging. Spectrum imaging is the collection of a full EDS X-ray spectrum at each pixel in an image. Once the maps are collected, it is possible to form chemical images. A SEM image of a region analyzed is shown in Fig. 9A, while the maps of phosphorus and sulfur are shown in Figs. 9B and 9C. It is apparent the phase associated with the crack is enriched in both these elements.

The second group of alloys is those with Cr_{eq}/Ni_{eq} ratios of ~1.74. In general, the solidification behavior of these alloys was different than those with lower Cr_{eq}/Ni_{eq} ratios, with the exception of Heat 9, which contained a higher level of S, 0.27%. The majority of the weld in Heat 9 also solidified as primary austenite, as did the two heats with the Cr_{eq}/Ni_{eq} ratio

of 1.55. An example of the microstructure showing the characteristic austenite solidified cellular dendritic structure is shown in Fig. 10A and at higher magnification in Fig. 10B along with several small intergranular solidification cracks. The fine grain structure is again apparent. The Weeter test results on this heat were similar to the circular welds and showed it was relatively resistant to cracking, although a few small cracks were observed, as shown in Fig. 10C. This sample was etched more lightly than the sample in Fig. 10B and clearly shows the solidification crack along an austenite grain boundary. Also apparent are darker etching grain boundaries that contain large quantities of sulfides.

The weld microstructures of the other two heats with a Cr_{eq}/Ni_{eq} ratio of 1.74 exhibited a different appearance. A repre-

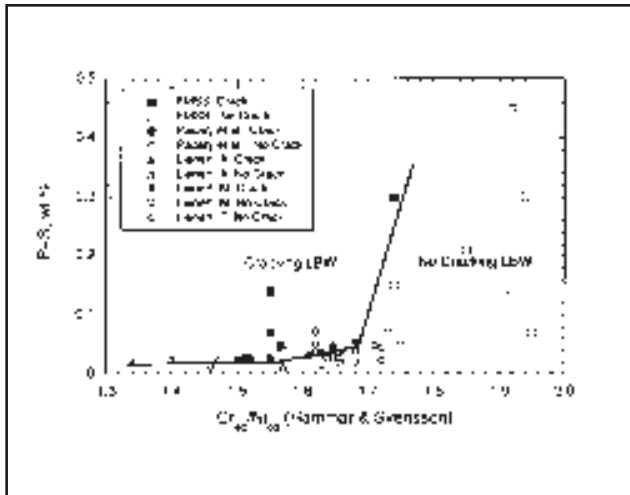


Fig. 6 — Plot of laser weld cracking behavior.

sentative microstructure is shown in Fig. 11A for Heat 3 with 0.04% sulfur. These welds contain isolated grains (primarily at the weld interface and interpulse boundaries) that exhibit the same cellular solidification structure as the laser welds in the low Cr_{eq}/Ni_{eq} ratio heats. However, the majority of the weld is composed of grains that exhibit little or no evidence of a solidification structure. Such a region is shown at higher magnification in Fig. 11B. It was concluded, as have other workers (Refs. 9, 12, 19, 23, 25), that grains that exhibited little segregation solidified as ferrite while grains or regions that clearly exhibited microsegregation or well-pronounced solidification cells solidified as austenite. It is also believed the ferrite solidified structure massively transformed to austenite during cooling leaving the weld completely austenitic. The rationale for this interpretation of the solidification behavior is discussed in more detail below.

The third group of alloys (with Cr_{eq}/Ni_{eq} ratios of ~1.85 to 1.95) solidified totally as ferrite and again contained no detectable residual ferrite in the optical, SEM, or TEM microscopes. The microstructure of Heat 2 ($Cr_{eq}/Ni_{eq} = 1.95$, $S = 0.04\%$) is shown at low magnification in Fig. 12A, and the overlapping laser pulses are clearly visible. The boundary regions are shown at higher magnification in Fig. 12B along with ferrite stringers in the base material. The weld microstructure of an alloy with a similarly high Cr_{eq}/Ni_{eq} ratio, but with high S content (Heat 6, $S = 0.42$), is shown in Fig. 13A. The low-magnification micrograph appears very similar to that shown in Fig. 12A, except it is much darker due to the high concentration of sulfides. The fusion zone boundary region is shown at higher magnification in Fig. 13B. In this micrograph, the sulfides are visible as spherical particles in the fusion zone, as large globules at the fusion zone

boundary, and as stringers (darker etching) in the base material. Laser welds of the alloys with the high Cr_{eq}/Ni_{eq} ratios were also studied in TEM. In samples with the lower sulfur levels, 0.04 wt-%, no sulfides were observed although some spherical oxides similar to those in Fig. 8 were noted. In the alloy containing the highest sulfur content, Heat 6, sulfides exhibit a bimodal distribution of submicron size particles, as shown in the TEM micrograph in Fig. 13C. Many of the larger particles in the solidified structure are comprised of amorphous aluminum oxide surrounded by Cr and Mn containing sulfides. The largest particles are contained in the solidification cell boundaries, although many of the particles are also present within the columnar dendritic structure. The smaller spherical sulfides noted in Fig. 13C are more uniformly distributed throughout the structure. It is likely these particles, ~200 angstroms in diameter, precipitated from the solid state during weld cooling. These smaller sulfides also contained primarily Mn and Cr. It is interesting that even with this high sulfide content, cracks were not observed in the weld structure.

The austenitic stainless steels are complicated by the transformation of austenite to ferrite at high temperature. Thus, in GTA welds that solidify as ferrite, a region of the HAZ from which solidification occurs can, depending upon alloy composi-

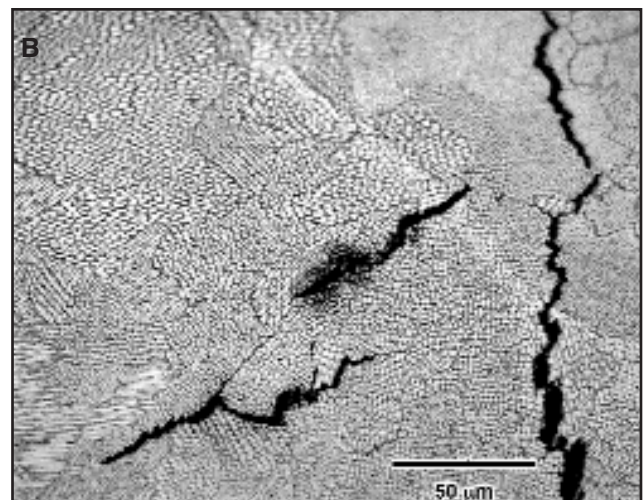
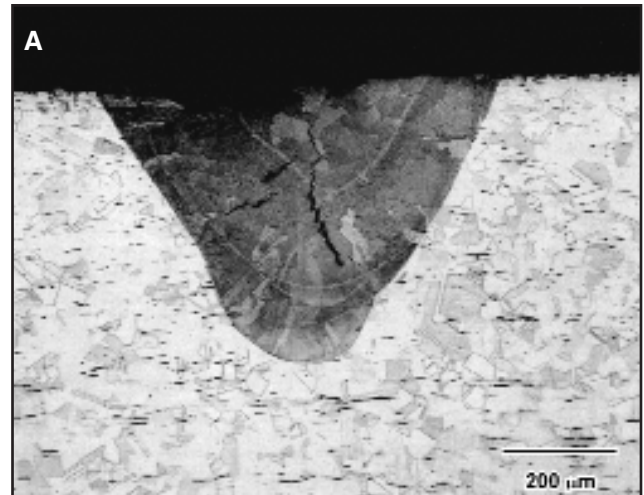


Fig. 7 — A — Laser weld of Heat 7 with a S content of 0.11% and a Cr_{eq}/Ni_{eq} ratio of 1.55; B — higher magnification of A showing distinct cellular-appearing primary austenite solidification structure and intergranular nature of cracks.

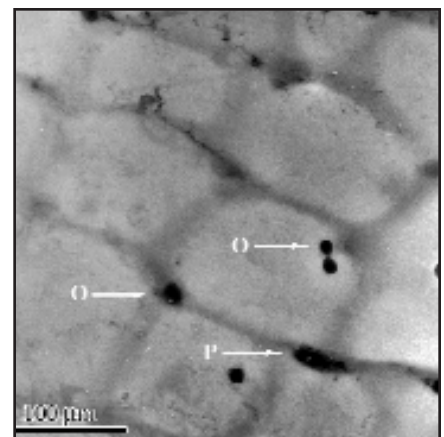


Fig. 8 — STEM image of laser weld in Heat 7 with a S content of 0.04% and a Cr_{eq}/Ni_{eq} ratio of 1.55 showing Al-containing oxides O and Cr-containing phosphides P.

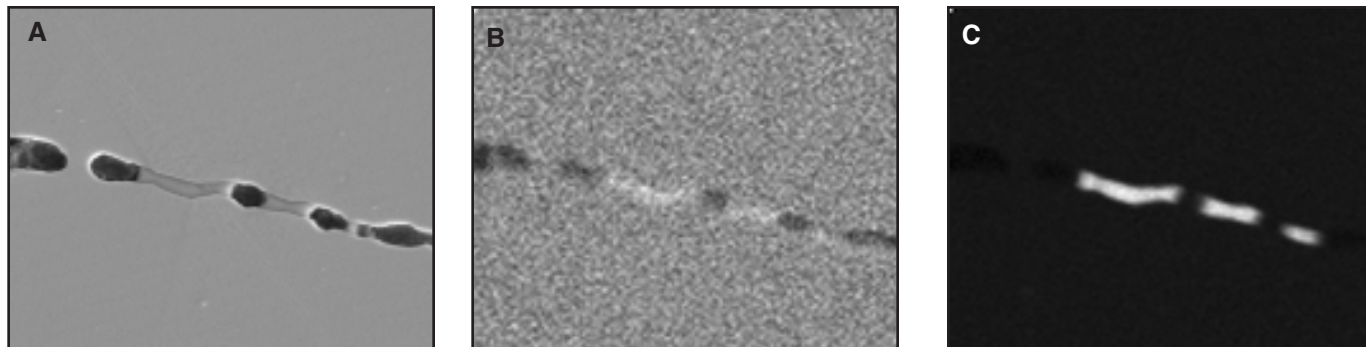


Fig. 9 — Position tagged spectroscopy results for laser beam weld in Heat 7 showing *A* — region of crack; *B* — phosphorus map; *C* — sulfur map. Constituent associated with crack is enriched in both elements.

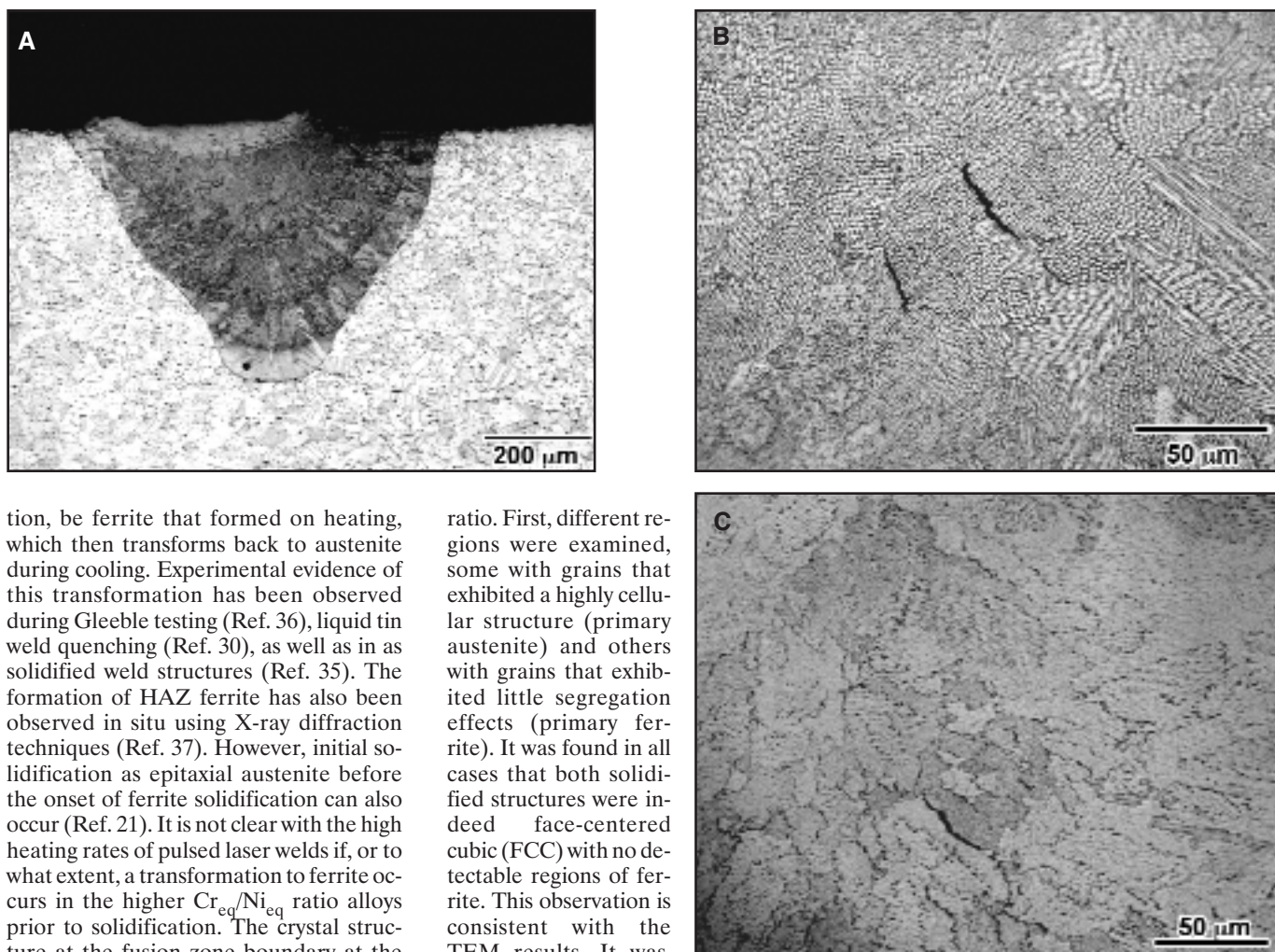


Fig. 10 — *A* — Microstructure of laser weld in Heat 9 with a *S* content of 0.27% and a Cr_{eq}/Ni_{eq} ratio of 1.74; *B* — higher magnification of *A* showing small cracks in the primary austenite solidified structure; *C* — microstructure of Heat 9 Weeter test sample showing crack at austenite grain boundary and sulfides along boundaries.

tion, be ferrite that formed on heating, which then transforms back to austenite during cooling. Experimental evidence of this transformation has been observed during Gleeble testing (Ref. 36), liquid tin weld quenching (Ref. 30), as well as in as solidified weld structures (Ref. 35). The formation of HAZ ferrite has also been observed in situ using X-ray diffraction techniques (Ref. 37). However, initial solidification as epitaxial austenite before the onset of ferrite solidification can also occur (Ref. 21). It is not clear with the high heating rates of pulsed laser welds if, or to what extent, a transformation to ferrite occurs in the higher Cr_{eq}/Ni_{eq} ratio alloys prior to solidification. The crystal structure at the fusion zone boundary at the time of solidification would have a major effect of the overall weld solidification behavior. To study this in more detail, electron backscattered diffraction (EBSD) analysis (Ref. 38) was used for both phase identification and to determine relative crystallographic orientations.

A number of fusion zone boundary regions were studied in Heat 3 (Cr_{eq}/Ni_{eq} ratio ~ 1.74). As shown in Fig. 11, a mix in solidification mode of ferrite and austenite was most apparent at this Cr_{eq}/Ni_{eq}

ratio. First, different regions were examined, some with grains that exhibited a highly cellular structure (primary austenite) and others with grains that exhibited little segregation effects (primary ferrite). It was found in all cases that both solidified structures were indeed face-centered cubic (FCC) with no detectable regions of ferrite. This observation is consistent with the TEM results. It was also found grains exhibiting the distinct cellular structure exhibited the same crystallographic orientation as the grain from which they grew, supporting the hypothesis that epitaxial growth of austenite from austenite had occurred. Moreover, similar behavior was observed at both base metal and inter-pulse weld interfaces. An example at an

interpulse boundary where the austenite diffraction patterns are the same in both regions is shown in Fig. 14. Regions were also examined where a cellular solidification region grew for a short distance be-

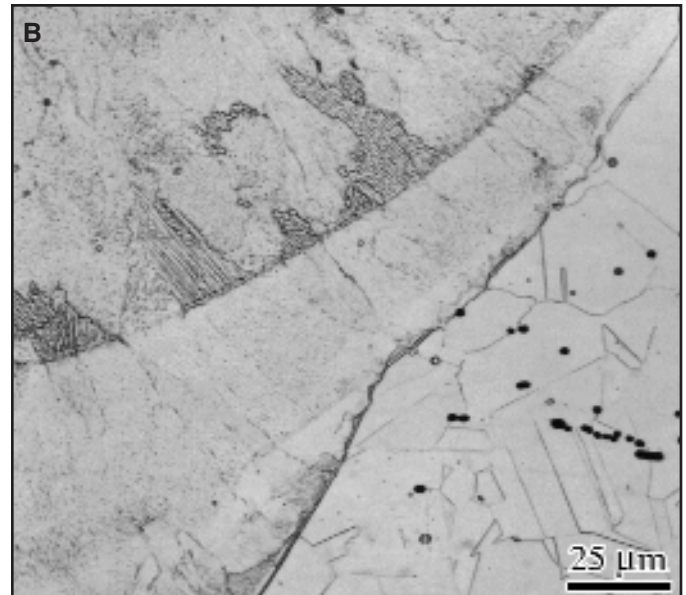
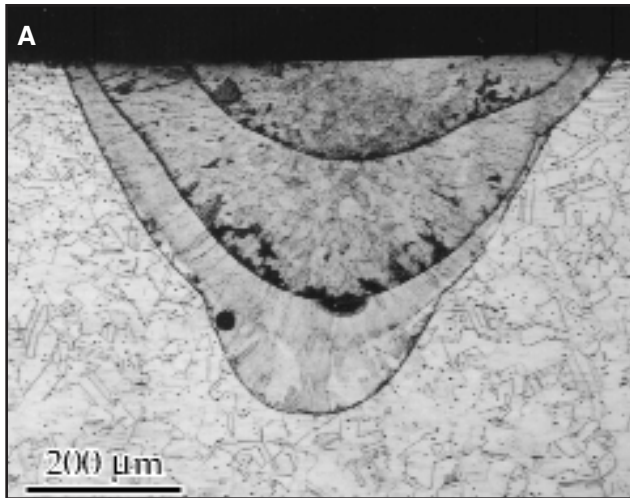


Fig. 11 —A — Microstructure of a laser beam weld in Heat 3 with an S content of 0.04% and a Cr_{eq}/Ni_{eq} ratio of 1.74 showing the nature of mixed mode solidification with austenite solidification (dark etching grains) generally confined to region of pulse weld boundaries; B — higher magnification of A taken in region of weld overlap.

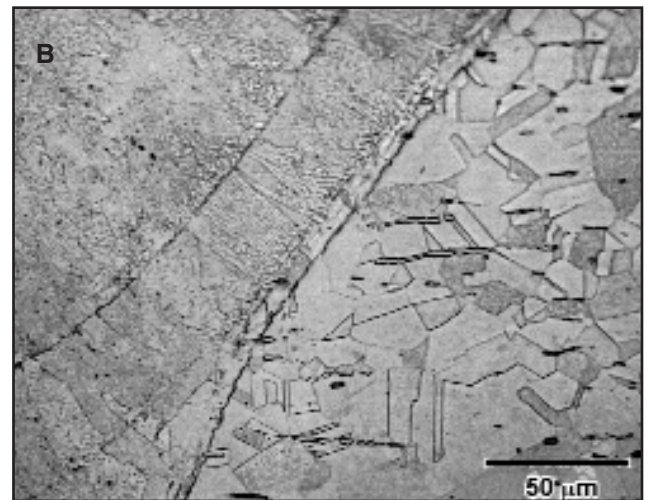
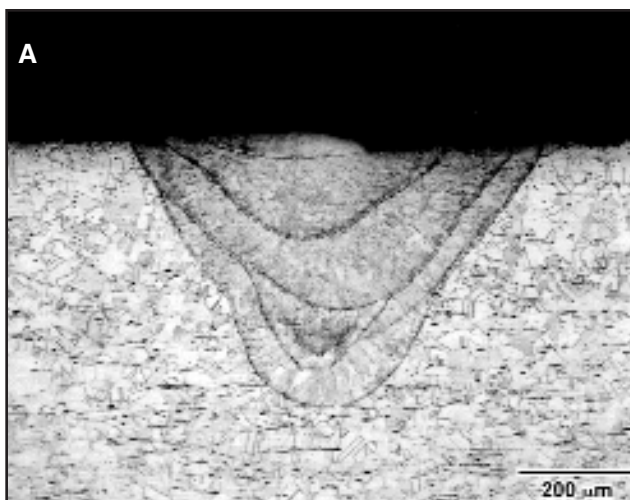


Fig. 12 —A — Microstructure of laser weld in Heat 2, $Cr_{eq}/Ni_{eq} = 1.95$, 0.04% S; B — higher magnification of boundary regions showing primary ferrite solidified structure.

fore leading into a more featureless (ferrite solidified) structure. Such a region is apparent in Fig. 15 in which the cellular structure again has the same orientation as the base grain. However, the featureless region only a few microns away has a different orientation, although microstructurally it appears to be within the same grain. The misorientation between the two regions (locations 5.1 and 5.2) within the weld is appreciable and is approximately equivalent to an 18.5-deg rotation about (212). This misorientation is greater than would be expected for a small angle boundary or stacking fault. The apparent growth of ferrite directly from the base

grain in which the base grain and solidified region have different austenite orientations is shown in Fig. 16.

In a similar manner, orientation maps were used to examine a large region of the fusion zone boundary. An example of primary austenite solidification is shown in Fig. 17A in which the sample was tilted 70 deg to obtain the Kikuchi patterns. Because of epitaxial growth, it is impossible from the map alone to determine the fusion zone boundary. It would seem the finer-appearing grain structure of the primary austenite welds in Fig. 7B is largely subgrains with only small orientation differences. The ferrite solidified welds are,

however, much different. Figure 17B shows the orientation imaging map of a weld in Heat 2 with a Cr_{eq}/Ni_{eq} ratio of 1.95. In this map the region of the fusion zone boundary is more apparent due to the differences in grain orientation. Considerably more grains are apparent on the fusion zone side of the boundary with relatively few cases where a single substrate grain corresponds to a single fusion zone grain. The grain size is also much smaller. Thus it appears that in the case of ferrite solidification, the nucleation and growth conditions are more complex, but consistent with the differences in microsegregation behavior.

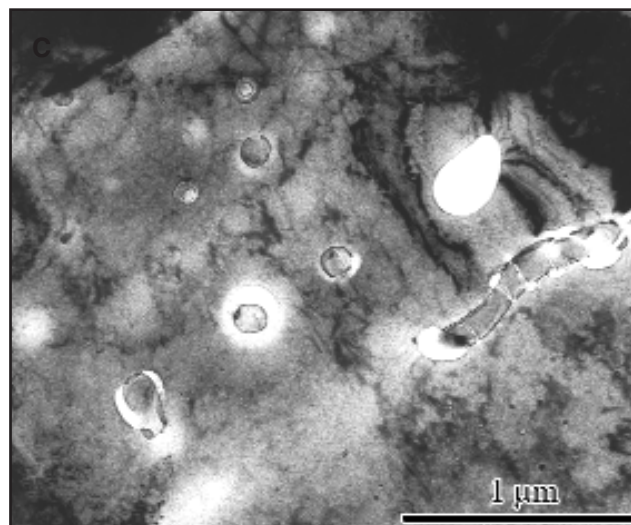
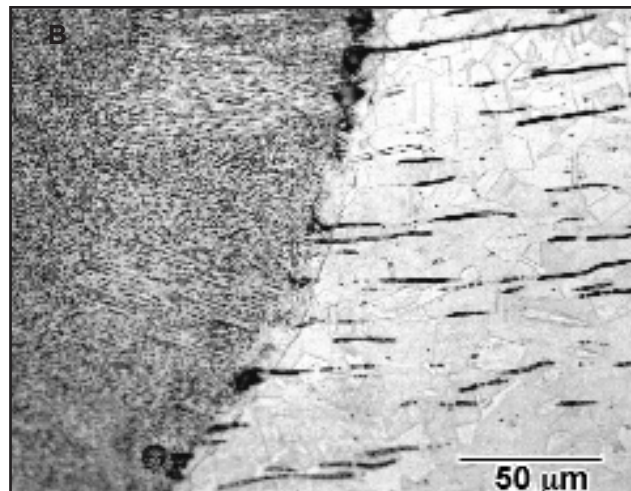
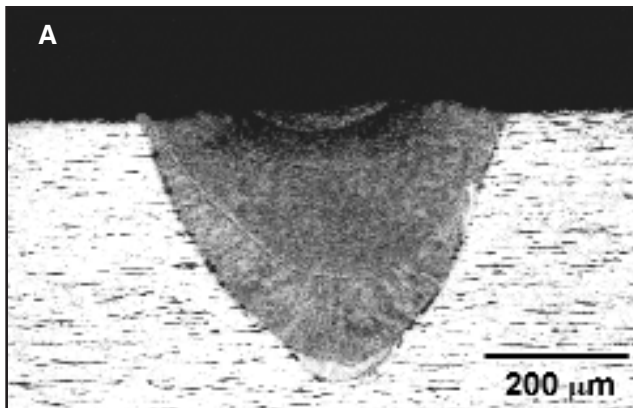


Fig. 13 — A — Microstructure of laser weld in Heat 6 with $Cr_{eq}/Ni_{eq} = 1.92$ and $0.42\% S$; B — boundary regions showing primary ferrite solidified structure containing high concentration of sulfides, globular sulfides at HAZ boundary, and sulfide and ferrite stringers in base material; C — TEM micrograph showing globular sulfides in solidification boundary, spherical Mn and Cr containing sulfides nucleated at amorphous aluminum oxide particles, and fine uniformly distributed sulfides.

Discussion

GTA Welds

It has been well established in conventional welds, such as GTA, that a strong correlation exists between solidification mode and weld cracking (Refs. 5, 9, 35, 39-42). Welds that solidify as primary ferrite with the secondary solidification of austenite, and welds that solidify totally as ferrite in which the transformation to austenite starts at a temperature near the solidus are extremely resistant to solidification cracking. Welds that solidify as austenite are very susceptible to cracking, although this susceptibility can be significantly reduced at low phosphorus and sulfur impurity levels. The transition in solidification mode from primary austenite to primary ferrite in low-speed GTA welds occurs at a Cr_{eq}/Ni_{eq} ratio ~ 1.5 when using Hammar and Svensson equivalents (Ref. 5) (~ 1.4 when using the WRC diagram). Similarly, welds that solidify totally as ferrite with a lower transformation temperature to austenite are also susceptible to cracking, although this behavior is not as well documented. This tendency for cracking at high Cr_{eq}/Ni_{eq} ratios has been reported by Kujampaa et al. (Ref. 35) to occur at Cr_{eq}/Ni_{eq} ratios above ~ 2.1 .

In examining the Varestraint data in Fig. 1, it can be seen the heat most susceptible to weld cracking is Heat 2 with the highest Cr_{eq}/Ni_{eq} ratio, 1.95, and the lowest sulfur content, 0.04 wt-%. The next most susceptible heats, 1, 7, and 4, all exhibited similar cracking behavior. Heats 1 and 7 both have a Cr_{eq}/Ni_{eq} ratio of 1.55 and sulfur levels of 0.04 and 0.11%, respectively. The third heat of this group, Heat 4, a Cr_{eq}/Ni_{eq} ratio of 1.92 and a sulfur level of 0.11 wt-%. The two heats that exhibited no cracking at any strain level were Heats 5 and 10 with Cr_{eq}/Ni_{eq} ratios of 1.94 and 1.85 and sulfur levels of 0.27 and 0.18%, respectively. The overall GTA Varestraint cracking behavior is summarized in Fig. 18 and plotted as (S+P) content vs. Cr_{eq}/Ni_{eq} ratio. In general, it can

be seen the data can be bound with a lower limit somewhat above 1.55 and a higher limit at ~ 1.9 . However, it was observed that the heats with the Cr_{eq}/Ni_{eq} ratio ~ 1.55 contained some regions solidified as austenite, primarily near the weld centerline, e.g., Fig. 3, Heat 7 with 0.11% sulfur. These regions were very susceptible to cracking. The transition in solidification from primary ferrite to primary austenite near the weld centerline has been reported previously in both GTAW (Ref. 43) and EBW processes (Ref. 44), and has been attributed to differences in dendrite tip velocity. In that work it was thought the solidification velocity was higher near the weld centerline — sufficiently high to exceed the critical dendrite tip velocity for the change in mode from primary ferrite to primary austenite. This type of behavior will typically occur at compositions near the critical Cr_{eq}/Ni_{eq} ratio of 1.5, and is likely the cause of the localized change in solidification mode observed here. However, it was also observed that in primary ferrite solidification regions of welds with the Cr_{eq}/Ni_{eq} ratio ~ 1.55 relatively severe cracking also occurred. This is somewhat surprising, but it could be seen that in the grain boundary regions of cracking, the local composition was sufficiently altered to promote primary austenite solidification (Ref. 42). This may be due partly to backfilling during straining with liquid sufficiently enriched with Ni and S to result in local primary austenite solidification —

Fig. 3B and 3C. It may be that at this high level of S, slightly higher Cr_{eq}/Ni_{eq} ratios, with a concomitant larger fraction of ferrite solidification, are required to significantly reduce cracking. It has been observed that in Fe-Ni-Cr ternary alloys at Cr_{eq}/Ni_{eq} ratios as high as ~ 1.6 , high levels of sulfur tended to promote austenite solidification and alter residual ferrite content (Ref. 45). In the alloys studied here, a higher Cr_{eq}/Ni_{eq} ratio of ~ 1.6 is needed to ensure good cracking resistance and may also be due to sulfur acting as a Ni equivalent.

The upper and lower bounds of the cracking susceptibility region shown in Fig. 18 are consistent with the work of Sutula and Kujanpää (Ref. 35). However, the limits are somewhat tightened, ~ 1.6 to 1.9, compared to their values of 1.5 to 2.1

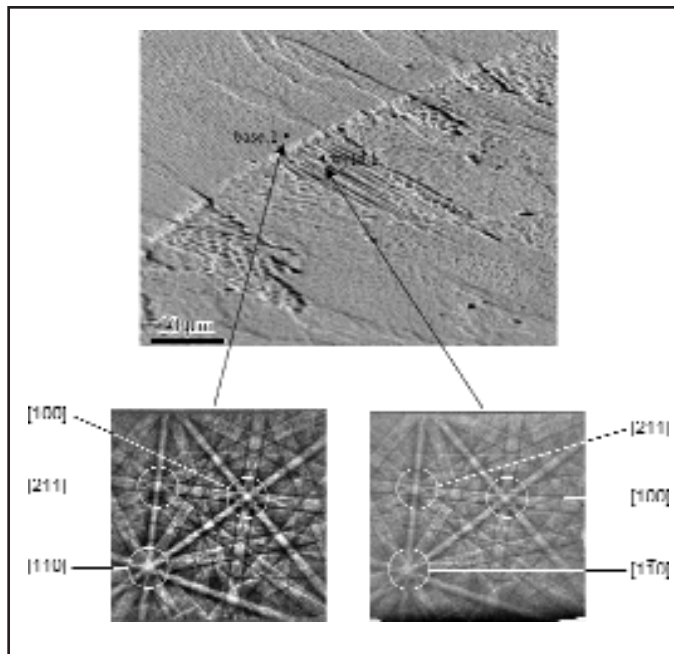


Fig. 14 — SEM micrograph with EBSD patterns showing epitaxial solidification of austenite at interpulse boundary. The EBSD patterns show both regions have same austenite orientation. (Heat 3, $Cr_{eq}/Ni_{eq} = 1.73$).

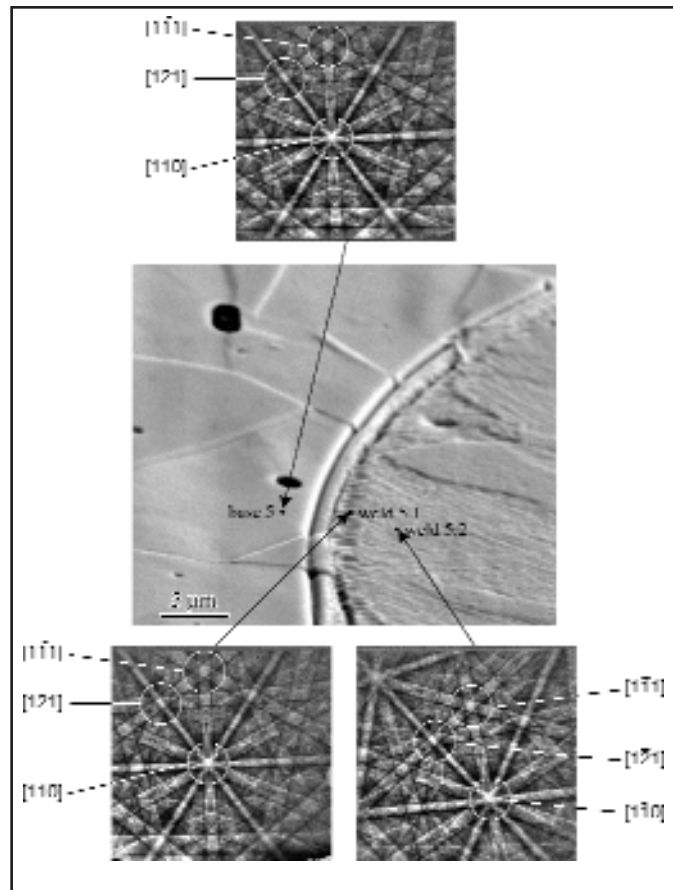


Fig. 15 — SEM micrograph showing cellular structure growing a short distance from the base material and changing to apparent featureless ferrite solidification. All EBSD patterns are FCC austenite, and show epitaxial solidification of austenite from base material with same orientation, while the orientation of the region that solidified as ferrite differs from the orientation of the base metal. (Heat 3).

(using Hammar and Svensson equivalents). The observed cracking at 1.55 is well within the data they compiled, especially considering the high levels of S and different testing techniques. The upper limit of 1.9 vs. 2.1 is significantly different and may also be related to weld test techniques. Since the change in cracking behavior is not associated simply with an abrupt change in solidification mode, as is the case of the lower bound of Cr_{eq}/Ni_{eq} ratio, it would be expected that the upper limit might not be as well defined. However, the change in cracking behavior is still related to solidification and solid-state transformation behavior. It is clear from the microstructures, with ferrite extending over a number of cell boundaries (Fig. 5A), that low S welds with Cr_{eq}/Ni_{eq} ratio of ~ 1.92 solidified completely as ferrite. Moreover, the morphology of the ferrite suggests the transformation of ferrite occurred at a temperature considerably below the solidus temperature (Refs. 9, 29, 30). The rationale summarized (Refs. 2, 9) to explain cracking behavior is consistent with the GTA weld data shown here. Solidification crack initiation and propagation along the complex interphase boundaries, formed during either ferrite-austenite solidification, or during the high-temperature transformation of primary ferrite to austenite, is more difficult than along the rather smooth, single-phase grain boundaries (Ref. 46). These single-phase boundaries occur at both the low Cr_{eq}/Ni_{eq} ratios with austenite solidi-

fication and at high Cr_{eq}/Ni_{eq} ratios where single-phase ferrite solidification predominates. Also, crack propagation may be more difficult along the lower surface energy δ - γ boundaries than along the higher energy δ - δ and γ - γ boundaries that are formed during solidification and cooling (Ref. 47).

The upper bound Cr_{eq}/Ni_{eq} ratio of ~ 1.9 for favorable cracking resistance also appears to be dependent upon sulfur content; i.e., the higher the sulfur level at a Cr_{eq}/Ni_{eq} ratio of ~ 1.93 , the greater the resistance to cracking. This behavior was also observed in ternary heats doped with high levels of sulfur (Ref. 2) and may be the result of backfilling from sulfur-containing eutectic liquid. In Fig. 3, it appears from the etching behavior the grain boundary regions (which did not form cracks) underwent considerable strain and contain large amounts of sulfides. These observations are consistent with a backfilling mechanism. However, it appeared microstructurally that higher levels of sulfur extended the range of two-phase F/A solidification to higher Cr_{eq}/Ni_{eq} ratios which would also improve cracking susceptibility. This is consistent with S altering the solidification mode at the lower ra-

tios of ~ 1.55 (Ref. 26).

It has been suggested the maximum crack length at the saturation strain level may be a better indicator of cracking behavior than the total crack length plotted against augmented strain. When analyzing Varestraint data, the saturation crack length at the highest strains corresponds to the temperature-sensitive region for cracking. The length of this region in a given weld is then directly related to the thermal gradient along the weld centerline (for a centerline crack) and the weld speed. The highest strain tested, 3.6%, may be close to the saturation strain. If this is the case, the maximum crack lengths at 3.6% strain in Table 2 would suggest Heat 2 is the most susceptible heat and this agrees with the total crack length data of Fig. 1. However, based on maximum crack length, the cracking behavior of Heats 4, 6, 7, and 9 should all be very similar and likely not that different from Heats 1 and 2. We believe the results in Figs. 1 and 18, rather than the maximum

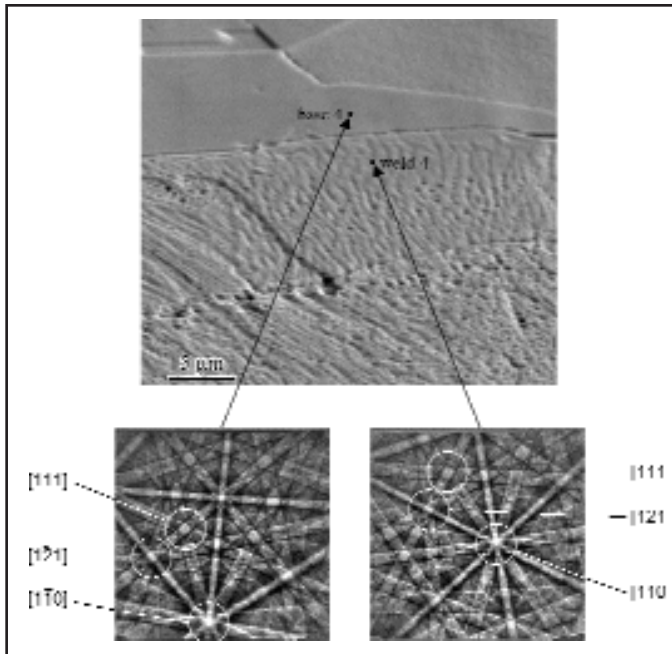


Fig. 16 — SEM micrograph with EBSD patterns showing solidification as ferrite from base grain. The EBSD patterns show different austenite orientations for the two regions. (Heat 3).

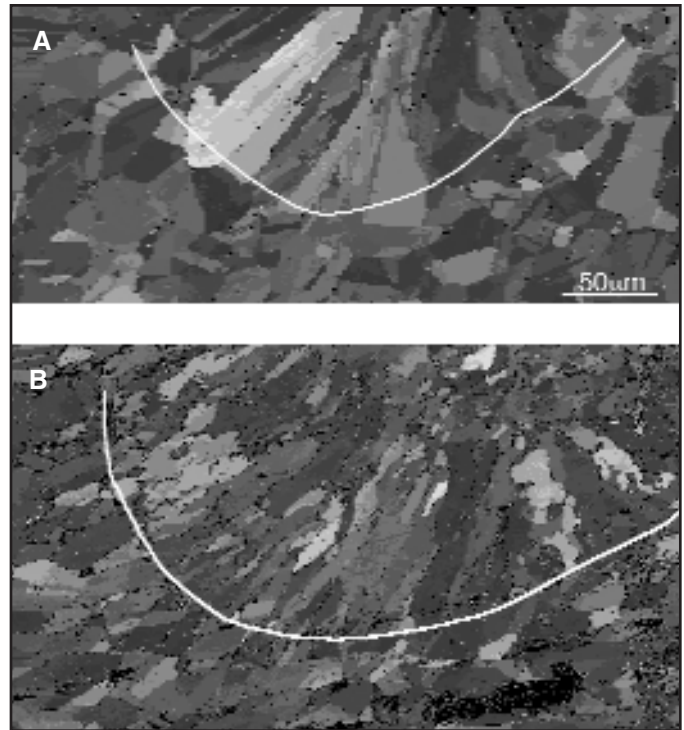


Fig. 17 — A — Orientation imaging map of primary austenite solidified laser weld of Heat 1. Note fusion zone boundary in map is not apparent due to epitaxial growth; B — similar map of Heat 2. Note orientation change across much of fusion zone boundary.

crack length at 3.6% strain, may be more representative of cracking response in production environments for the heats of material studied here.

Laser Beam Welds

Before discussing the solidification cracking behavior of the laser beam welds, or correlating solidification cracking behavior to solidification mode, one must be able to distinguish between the two primary modes of solidification. No weld ferrite was present that could more clearly define solidification behavior. We concluded the weld regions that exhibited the distinct cellular dendritic structure solidified as primary austenite while those regions that exhibited little or no evidence of the cellular solidification structure solidified as ferrite. These conclusions were based on earlier studies that showed the combined effect of dendrite tip undercooling and solid-state diffusion is much more effective in reducing microsegregation during ferrite solidification than in austenite solidification (Refs. 14, 15). However, other workers have proposed that the segregation-free, high-energy-density laser welds may be the result of partitionless solidification (Ref. 13). In either case, the use of EBSD further supported the relationship between the pri-

mary phase of solidification and the degree of microsegregation

There appeared to be three different types of initial solidification behavior of the laser welds, similar to those reported by Lippold (Ref. 23). The first was the initial epitaxial growth and continuing solidification of austenite. The second was the initial epitaxial growth of austenite followed by a transition to ferrite solidification within a distance of only a few microns. Both behaviors existed with a Cr_{eq}/Ni_{eq} ratio of 1.74 at the lower sulfur levels. The difference in the two behaviors may be related to the crystallographic orientation of the substrate grain and the direction of maximum heat flow. If the individual grains solidify at a rate near that of the macroscopic solidification front, then dendrites within different grains must grow at different velocities. Dendrites in grains with a $\langle 100 \rangle$ direction aligned along that of maximum heat flow (normal to the macroscopic solid/liquid interface) will grow at a slower rate than dendrites within grains with significant misalignment. Dendrites in these less favorably aligned grains must travel further, and thus faster, to maintain the velocity of the macroscopic solidification front. However, their tips will also be at a lower temperature and lag those in an adjacent, more favorably oriented, grain (Ref. 48).

These grains may then be cut off during the commonly observed competitive growth process. In stainless steel laser welds, when the macroscopic interface velocity is near that of the critical transition velocity for $\delta \rightarrow \gamma$ solidification (Cr_{eq}/Ni_{eq} ratio ~ 1.7 in this study), the increased dendrite growth velocity in less favorably aligned grains may promote austenite solidification. When the growth direction is more favorably aligned and dendrite tip velocities are slower, a transition from initial solidification of austenite to the growth of ferrite will occur. However, growth of ferrite will first require nucleation. As a result, the transition to ferrite solidification will occur for velocities somewhat slower than that of the commonly calculated critical transition velocity (Ref. 15).

The third condition appeared to be direct solidification of ferrite from the substrate. This was the common mode at the higher Cr_{eq}/Ni_{eq} ratios ~ 1.9 . There appeared to be no precursor solidification of austenite, and the austenite orientations were usually different across the interface. It also appeared in many cases that a single grain of ferrite solidified from a single substrate grain — Fig. 16. This suggests the fusion zone boundary region was ferrite at the time of initial solidification, possibly as a result of a massive transforma-

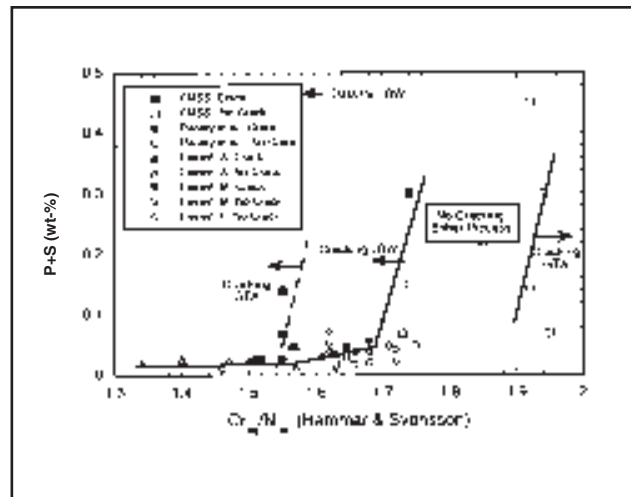
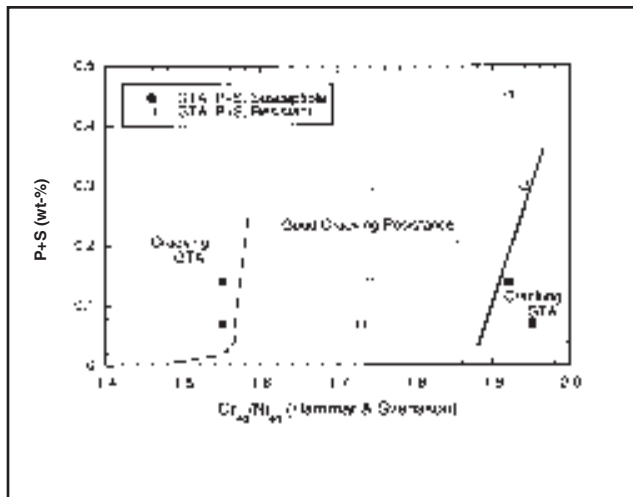


Fig. 18 — Summary of GTA weld results showing region of good solidification cracking resistance.

Fig. 19 — Combined results of both GTA and pulsed laser welds (Figs. 6 and 18) showing a region of good weldability limited by LBW at low Cr_{eq}/Ni_{eq} ratios and by GTA at high ratios. Note that only LBW data is shown.

tion on heating. If ferrite nucleated at the austenite interface during initial solidification, numerous grains may coincide with individual substrate grains unless ferrite nucleated on austenite with a preferred, low-energy configuration. Low-energy orientations between ferrite and austenite established during both solidification (Refs. 49, 50) and solid-state transformations (Ref. 9) have been observed in stainless steel welds. The EBSD patterns in Fig. 17B covering a large region of the weld show the FZ boundary region consists of more grains than that of the corresponding substrate. However, this is primarily a result of the solidified ferrite massively transforming to austenite, yielding a finer grain structure than that of the parent ferrite grain, which complicates interpretation of the solidification behavior (Ref. 51). It is also possible the massive transformation could initiate at the austenite fusion and interpass boundaries, resulting in no orientation change across the boundary; this was not commonly observed. It is evident initial solidification of ferrite in the pulsed laser welds is complex and needs further study. Nevertheless, the use of segregation patterns to distinguish solidification mode, which is important for this study, is consistent with the crystallographic orientations observed for the different structures.

Irrespective of the details of the solidification mechanics, it was found only welds that solidified as primary austenite exhibited weld cracking. This behavior is consistent with earlier results on pulsed laser welds with lower levels of phosphorus and sulfur (Refs. 22–24). Our data is also consistent with previous work that indicates the change in solidification mode

due to dendrite tip undercooling occurs at a Cr_{eq}/Ni_{eq} ratio of about 1.68–1.7. The line in Fig. 6 separating cracking from no cracking for Cr_{eq}/Ni_{eq} ratios below ~1.7 was defined by the data of Pacary et al. and Lienert. In the Cr_{eq}/Ni_{eq} ratio range between ~1.6 and 1.7, their welds often exhibited mixed modes of solidification of ferrite and austenite. Pacary et al. showed a vertical line separating cracking and no cracking at ~1.67 and Lienert at 1.7. Those lines generally corresponded to the transition to nearly complete ferrite solidification. However, we found that with a Cr_{eq}/Ni_{eq} ratio of 1.74, the welds still solidified in a mixed mode, although the fraction of primary ferrite solidification was typically high, ~75% or greater. An exception was Heat 9 with the highest amount of sulfur (0.27%), in which a large fraction of the weld solidified as primary austenite. In this heat, however, only a small amount of cracking was observed. In this heat, the solidified grain boundaries contained large amounts of sulfides, which implies sufficient eutectic liquid was available to heal or prevent the formation of nearly all cracks in a manner similar to the GTA welds in Heat 6. In Fig. 6, it is primarily the results from this heat that led us to incorporate the sulfur dependence at the higher Cr_{eq}/Ni_{eq} ratio of ~1.7. It is not clear why the solidification behavior of Heat 9 is different than the other heats with the same Cr_{eq}/Ni_{eq} ratio, but, as with the GTA welds, S appears to be playing a role as an apparent austenite former. The mixed mode solidification behavior of the other two heats with Cr_{eq}/Ni_{eq} ratios of ~1.74 is also different than the single-phase ferrite mode observed by Lienert, see Fig. 6. These differences further sug-

gest the possible role of sulfur in solidification behavior. However, it should be noted similar discrepancies in solidification mode at constant Cr_{eq}/Ni_{eq} ratios were also observed in another study involving austenitic stainless steels and electron beam welds (Ref. 20), although in the current study, the basic compositions are almost identical except for sulfur. Differences in weld parameters between the different studies discussed here may also be playing a role in solidification behavior (Ref. 52).

In light of the GTA V restraint test results, it is interesting to note the laser welds with the highest Cr_{eq}/Ni_{eq} ratios seemed resistant to cracking. This lack of cracking is inconsistent with the hypothesis that cracking susceptibility is high for single-phase ferrite solidification when the transformation to austenite occurs at lower temperatures, as it would for a massive transformation. It was evident that even though the solubility of sulfur is higher in ferrite than in austenite, a large amount of sulfides still formed during solidification. Since no cracking was observed at any level of sulfur tested, a simple eutectic healing mechanism cannot be invoked.

In one of the heats with the lowest Cr_{eq}/Ni_{eq} ratio that solidified as austenite and exhibited extensive cracking (Heat 7), it was found low melting phases associated with the cracks contained both sulfur and phosphorus — Fig. 9. The sulfur content of this heat was 0.11%. However, sulfides were not observed in TEM in the austenite solidified welds of Heat 1 with the lower sulfur level, which still exhibited severe cracking. Thus, it is conceivable phosphorus is primarily responsible for crack-

ing and not sulfur. The phosphorus content of all the heats was relatively high, 0.03%. Given the higher phosphorus solubility in ferrite than austenite, higher levels of phosphorus may be tolerated in those heats solidifying as ferrite. In addition, the finer grain size of primary ferrite solidification (Fig. 17) should also reduce the tendency for cracking.

The results of the GTA and laser welding trials can be combined to describe alloy compositions that are amenable to welding with either conventional or HED processes. This combination is shown in the summary plot of Fig. 19. As shown, a lower weldability limit occurs at a Cr_{eq}/Ni_{eq} ratio of ~ 1.7 and is established by the laser weld process, while the upper weldability limit of ~ 1.9 is established by the GTA process. The boundaries at these limits are sloped, which implies the limits are somewhat dependent upon sulfur content, although additional data is desirable. As discussed earlier, it is important to emphasize that although the data is portrayed in terms of total impurity level (P+S), it should be remembered this portrayal is based more on convention than a strong experimental or theoretical basis. Nevertheless, Fig. 19 illustrates reasonable fabrication weldability can probably be achieved in free-machining grades through suitable choice of alloy composition. The mechanical properties of GTA, EB, and laser beam welds in these alloys are reported elsewhere (Refs. 25, 26).

Summary

The cracking response of GTA welds was controlled primarily by solidification mode. Using Suutula equivalents, the lower bound of Cr_{eq}/Ni_{eq} ratio for good cracking resistance was ~ 1.6 , while the upper bound was ~ 1.9 . This response is consistent with existing rationale for describing solidification cracking behavior of austenitic stainless steels. However, at the upper limit, high sulfur appeared to reduce the cracking susceptibility of the single-phase ferrite solidified welds. This reduction may be attributed to eutectic healing involving sulfur-containing-liquid and/or a change in solidification mode due to sulfur acting as a Ni_{eq} . The exact role of sulfur appears to be complex. It was somewhat surprising the heat with the highest Cr_{eq}/Ni_{eq} ratio and the lowest level of sulfur was the most susceptible to GTA weld cracking.

The solidification behavior of pulsed laser welds was also generally related to Cr_{eq}/Ni_{eq} ratio. However, solidification in the laser welds is complex, and in many cases the welds exhibited mixed mode solidification behavior. As with the GTA welds, the solidification cracking behavior

of the laser welds was related to solidification mode. At Cr_{eq}/Ni_{eq} ratios of 1.55, welds solidified as austenite and were susceptible to cracking. Welds in alloys with Cr_{eq}/Ni_{eq} ratios of 1.74 solidified in a mixed mode, with some regions solidifying as ferrite and other regions as austenite, but, in general, appeared to exhibit good cracking resistance. However, with the same Cr_{eq}/Ni_{eq} ratio but a higher level of sulfur, 0.27%, the amount of austenite solidification increased and a small amount of cracking was observed. At the Cr_{eq}/Ni_{eq} ratios of 1.92, the welds solidified completely as ferrite, but, unlike the GTA welds, the resistance to cracking was high at all impurity contents. In the laser welds, phosphorus is likely to play a major role in weld cracking behavior. For the alloys studied, good cracking resistance was observed within a range of Cr_{eq}/Ni_{eq} ratios of ~ 1.7 to 1.9, with the lower limit established by the laser process and the upper limit established by the GTA cracking behavior.

Acknowledgments

Special thanks are given to Andy Gardea for metallographic services and to Annette Newman for laboratory support on weldability testing. Thanks are also given to Jerry Knorovsky for initial assessment of the laser weld performance and to Mike Cieslak for reviewing the manuscript. The experimental alloys were produced by Carpenter Technology Corp., and its participation is greatly appreciated. Sandia is a multiprogram laboratory operated by Sandia Corp., a Lockheed Martin company, for the United States Department on Energy under Contract DE-AC04-94AL85000.

References

- Lundin, C. D., Lee, C. H., and Menon, R. 1988. Hot ductility and weldability of free machining austenitic stainless steel. *Welding Journal* 67(6): 122-s to 130-s.
- Brooks, J. A., Thompson, A. W., and Williams, J. C. 1984. A fundamental study of the beneficial effect of delta ferrite in reducing weld cracking. *Welding Journal* 63(2): 71-s to 83-s.
- Kotecki, D., and Siewert, T. A. 1992. WRC-1992 constitution diagram for stainless steel weld metals: A modification to the WRC-1988 diagram. *Welding Journal* 71(5): 171-s to 179-s.
- Suutula, N. 1982. Effect of solidification conditions on the solidification mode in austenitic stainless steels. *Acta Universitatis Ouluensis, Series C Technica*, No. 23. University of Oulu, Oulu, Finland.
- Takalo, T., Suutula, N., and Moisio, T. 1979. Austenitic solidification mode in austenitic stainless steel welds. *Metall. Trans.* 10A(4): 1173-1181.
- Olson D. L. 1985. Prediction of austenitic weld metal microstructure and properties. *Welding Journal* 64(11): 181-s to 295-s.
- Hammar, Ö., and Svensson, U. 1979. Influence of steel composition on segregation and microstructure during solidification of austenitic stainless steels. *Solidification and Casting of Metals*. London, England: The Metals Society, pp. 401-410.
- Kurz, W., and Fisher, D. J. 1989. *Fundamentals of Solidification*. Switzerland: Trans Tech Publications Ltd.
- Brooks, J. A., and Thompson, A. W. 1991. Microstructural development and solidification cracking susceptibility of austenitic stainless steel welds. *International Materials Reviews* 36(1): 16-44.
- David, S. A., and Vitek, J. M. 1981. Solidification behavior and microstructural analysis of austenitic stainless steel laser welds. *Lasers in Metallurgy*, K. Mukherjee and J. Mazumder, eds. Warrendale, Pa.: TMS-AIME, pp. 247-254.
- Vitek, J. M., Dasgupta, A., and David, S. A. 1983. Microstructural modification of austenitic stainless steels by rapid solidification. *Metall. Trans A* 14A: 1833-1841.
- Katayama, S., and Matsunawa. 1985. Solidification microstructures of laser welded stainless steels. *Proc. ICALEO '84*. Toledo, Ohio: Laser Institute of America, pp. 60-67.
- Elmer, J. W. 1992. Nonequilibrium microstructures produced during electron-beam and laser-beam surface modification of metallic alloys. *The Metals Science of Joining*, Cieslak, Perepezko, Kang, and Glicksman, eds. Warrendale, Pa.: TMS, , pp. 123-133.
- Brooks, J. A., and Baskes, M. I. 1989. Microstructural modeling and transformation in rapidly solidified austenitic stainless steel welds. *Proc. of 2nd International Conf. Trends in Welding Research*, S. David and J. Vitek, eds. Materials Park: ASM International, Ohio, pp. 158-63.
- Brooks, J. A., Baskes, M. I., and Greulich, F. A. 1991. Solidification modeling and solid state transformations in high-energy density welds. *Metall. Trans.* 22A: 915-925.
- Fukumoto, S., and Kurz, W. 1997. The δ - γ transition in Fe-Cr-Ni alloys during laser treatment. *ISIJ International* 37 (7): 677-684.
- Elmer, J. W., Allen, S. M., and Eagar, T. W. 1989. Microstructural development during solidification of stainless steel alloys. *Metall. Trans* 20A: 2117-2131.
- David, S. A., Vitek, J. M., and Hubble, T. L. 1987. Effect of rapid solidification on stainless steel microstructures and its implication on the Schaeffler diagram. *Welding Journal* 66(10): 289-s.
- Nakao, Y., Nishimoto, K., and Zhang, W. 1988: Effects of rapid solidification by laser surface melting on solidification modes and microstructure of stainless steel. *Trans. JWJI* 19:101.
- Laursen, B., Olsen, F., Yardy, J., and

Funder-Kristensen, T. 1997. Experimental determination of the primary solidification phase dependency on the solidification velocity of 17 different stainless steel compositions. *Proceedings ASM International Conference on Welding and Joining Science and Technology*, Madrid Spain, pp. 571-580.

21. Inoue, H., Koseki, T., Ohkita, S., and Tanaka, T. Effect of solidification and subsequent ferrite-to-austenite massive transformation in an austenitic stainless steel weld metal. *ISIJ*, pp. 1248-1257.

22. Pacary, G., Moline, M., and Lippold, J. C. 1990. A diagram for predicting the weld solidification cracking susceptibility of pulsed-laser welds in austenitic stainless steel. *EWI Research Brief No. B9008*. Columbus, Ohio: Edison Welding Institute.

23. Lippold, J. C. 1994. Solidification behavior and cracking susceptibility of pulsed-laser welds in austenitic stainless steel. *Welding Journal* 73(6): 129-s to 139-s.

24. Lienert, T. J. 1998. A combined PSM/weldability diagram for laser welded austenitic stainless steels. *Proc. 5th International Conf. Trends in Welding Research*, Materials Park, Ohio: ASM International, pp. 724-728.

25. Brooks, J., Goods, S., Yang, N., Robino, C., and Headley, T. 1999. Solidification and weldability of free machining stainless steel. *International Conference on Joining of Advanced and Specialty Materials*. Cincinnati, Ohio: ASM, pp. 209-216.

26. Brooks, J. A., Goods, S. H., and Robino, C. V. Weld properties of AISI 303 free machining stainless steel. To be published in the April 2003 *Welding Journal*.

27. Campbell, R. D., and Walsh, D. W. 1993. Weldability testing. *ASM Handbook*, Vol. 2, pp. 603.

28. Weeter, L. A., Albright, C. E., and Jones, W. H. 1986. Development of a weldability test for pulsed laser beam welds. *Welding Journal* 65(8): 51-s to 62-s.

29. Suutula, N., Takalo, T., and Moision, T. 1979. Relationship between solidification and microstructure in austenitic and austenitic-ferritic stainless steel welds. *Metall. Trans A* 10A(4): 512-514

30. Brooks, J. A., Yang, N., and Krafcik, J. 1992. On the origin of ferrite morphologies of primary ferrite solidified austenitic stainless steel welds. *Trends In Welding Science and Technology*, S. A. David and J. M. Vitek, eds. Materials Park, Ohio: ASM International, pp. 173-180.

31. Borland, J. C., and Younger, R. N. 1960. Some aspects of cracking in welded Cr-Ni austenitic steels. *British Welding Journal*, Vol. 7, pp. 22-59.

32. Brooks, J. A., and Lambert, Jr., F. J., 1978. The effect of phosphorus and sulfur and ferrite content on weld cracking of type 309 stainless steel. *Welding Journal* 51(5): 139-s.

33. Brooks, J. A. 1975. Weldability of high N, high Mn austenitic stainless steel. *Welding*

Journal 54(6): 189-s to 195-s.

34. Li, L., and Messler, Jr., R. W. 1999. The effects of phosphorus and sulfur on susceptibility to weld hot cracking in austenitic stainless steels. *Welding Journal* 78(12): 387-s to 396-s.

35. Kujanpää, V., Suutala, N., Takalo, T., and Moision, T. 1979. Correlation between solidification cracking and microstructure in austenitic and austenitic-ferritic stainless steel welds. *Welding Research Int.* 9(2): 55-75.

36. Hee-Sung Ann, Chi-Seung Park, Byung-Chul Kim, and Jong-Hyun Park. 1989. Proposal of solidification sequences and microstructure characterization in dissimilar welds. *Trends in Welding Science and Technology*. S. A. David and J. M. Vitek, eds. Materials Park, Ohio: ASM International, pp. 257-262.

37. Elmer, J. W., Wong, J., and Ressler, T. 1999. Direct observation of phase transformations in austenitic stainless steel welds using in-situ spatially resolved and time resolved X-ray diffraction. *The Second International Symposium on the Joining of Advanced Materials ASM Materials Solutions '99*, Cincinnati, Ohio.

38. Schwarzer, R. A. 1997. Automated crystal lattice orientation mapping using a computer controlled SEM. *Micron* 28(3): 249-265.

39. Thier, H. 1976. Delta-Ferrite and hot cracking during the welding of chemically resistant austenitic steels. *DVS-Berichte*, no. 41, pp. 100-104.

40. Masumoto, I., Tamaki, K., and Kutsuna, M. 1972. Hot cracking of austenitic stainless steel weld metal. *Trans. JWS*, 41(11): 1306.

41. Arata, J., Matsuda, F., and Katayama, S. 1976. Fundamental investigation on solidification behavior of fully austenitic and duplex structures and effect of ferrite on microsegregation. *Trans. JWRI* 5(2): 35.

42. Lippold, J. C. 1982. Weld cracking mechanism in austenitic stainless steels. *Trends in Welding Research Conference Proceedings*, Metals Park, Ohio: ASM International, pp. 209-247.

43. Brooks, J.A., Thompson, A.W., Williams, J.C. 1980. Weld cracking of austenitic stainless steels — effects of impurities and minor elements. *Physical Metallurgy of Metal Joining*, R. Kossowsky and M. Glicksman, eds. Warrendale, Pa.: TMS-AIME, pp 117-136.

44. Lippold, J.C. 1985. Centerline cracking in deep penetration electron beam welds in type 304L stainless steel. *Welding Journal* 64(5): 127-s to 136-s.

45. Brooks, J. A., Thompson, A. W., and Williams, J. C. 1983. Variations in weld ferrite content due to P and S. *Welding Journal* 72(8): 220-s to 225-s.

46. Matsuda, F., Nakagawa, H., Uehara, T., Kaatayama, S., and Arata, Y. 1979. A new explanation for role of delta-ferrite improving solidification crack susceptibility in austenitic stainless steel. *Journal JWRI* 8(1): 105-112.

47. Hull, F. C. 1967. Effect of delta ferrite on hot cracking of stainless steel. *Welding Journal* 46(9): 399-s to 409-s.

48. Li, M., and Brooks, J. A. 1998. Mecha-

nism of single centerline grain formation in titanium alloy welds. *Science and Tech. of Welding and Joining* 3(2): 89-96.

49. Inoue, H., Koseki, T., Okita, S., and Fuji, M. 1997. Solidification and transformation behavior of austenitic stainless steel weld metals solidified as primary ferrite: Study of solidification and subsequent transformation of Cr-Ni stainless steel weld metals. *Welding Inter.* 11(12): 937-949.

50. Headley, T. J., and Brooks, J. A. 1992. A new Bcc-Fcc orientation relationship observed between ferrite and austenite in solidification structures of steel. *Metall. Trans. A* 33(1): 5-15.

51. Katayama, S., Matsunawa, A., and Iamboliev, T. 1998. Formation mechanism of rapidly quenched microstructure of laser weld metals in austenitic stainless steels. *Proc. 5th Intern. Conf. on Trends in Welding Research*, Materials Park, Ohio: ASM International, pp. 93-98.

52. Yardy, J., Laursen, B. 1995. Weld pool microstructures in pulsed-laser welded austenitic stainless steels. *Proc. 4th International Conf. on Trends in Welding Research*, pp. 165-170.

REPRINTS REPRINTS

To order custom reprints of
articles in

Welding Journal

Contact Denis Mulligan at

(800) 259-0470

FAX: (717) 481-7677

or via e-mail at

info@reprintdept.com

REPRINTS REPRINTS